Nanoscale Advances

Accepted Manuscript

This article can be cited before page numbers have been issued, to do this please use: A. USHKOV, N. Belozerova, G. Tikhonowski, S. Klimov, A. V. Syuy, S. Bazhenov, S. Novikov, V. G. Leiman, A. V. Arsenin, G. Celikov and V. Volkov, *Nanoscale Adv.*, 2026, DOI: 10.1039/D6NA00119J.

ROYAL SOCIETY OF CHEMISTRY

rsc.li/nanoscale-advances

View Article Online
DOI: 10.1039/D6NA00119J

Journal Name

ARTICLE TYPE

Cite this: DOI: 00.0000/xxxxxxxxxx

Solvent-Directed Femtosecond Laser Ablation: Tuning Phase and Defect Engineering in Hybrid $CdPS_3$/CdS Nanostructures

Andrei Ushkov,*[a] Nadezhda Belozerova,[a,b] Gleb Tikhonowski, [c] Stepan Klimov, [a] Alexander Syuy, [a,c,d] Sergey V. Bazhenov, [a] Sergey Novikov, [a] Vladimir G. Leiman, [a] Aleksey Arsenin, [a,c] Gleb I. Tselikov, [c] and Valentyn Volkov[c]

Received Date
Accepted Date

DOI: 00.0000/xxxxxxxxxx

The limited visible-light absorption of wide-bandgap van der Waals crystals fundamentally restricts their utility in solar energy conversion. Here, we report the application of a surfactant-free, solvent-directed laser synthesis strategy to engineer the phase and optoelectronic properties of Cadmium Phosphorus Trisulfide ($CdPS_3$). By exploiting the non-equilibrium thermodynamics of femtosecond pulsed laser ablation in liquid (fs-PLAL), we demonstrate a tunable transition from the stoichiometric ternary phase to a highly active binary-rich heterostructure. While ablation in water preserves the monoclinic $CdPS_3$ lattice, the reducing environment of isopropanol triggers the formation of CdS quantum dots and metallic cadmium defect sites. This solvent-induced phase engineering transforms the ultraviolet-active host into a robust visible-light photocatalyst. The resulting hybrid $CdPS_3$/CdS nanocolloids exhibit superior charge separation efficiency, driven by Schottky-like metal-semiconductor junctions, achieving $\sim$ 90% degradation of Methylene Blue under 532 nm irradiation within 30 minutes. This work establishes fs-PLAL as a scalable defect-engineering tool for complex ternary layered materials, offering a new design of high-performance metal-thiophosphate-based photocatalysts.

1 Introduction

The global efforts toward sustainable energy and environmental remediation requires the development of advanced functional materials for highly-efficient solar energy harvesting. Semiconductor photocatalysts was found to be simultaneously efficient for water purification and green hydrogen production [1–3]. However, conventional metal oxides (e.g., TiO_2, ZnO) are constrained by wide bandgaps that limit their operation to the ultraviolet (UV) region. Consequently, the search for visible-light-active semiconductors with tunable electronic structures and high specific surface area is highly demanded, directing attention toward the family of two-dimensional (2D) transition metal phosphorus trichalcogenides (MPX_3) [4,5].

Among these van der Waals (vdW) antiferromagnets, Cadmium Phosphorus Trisulfide ($CdPS_3$) stands out for its unique structural framework, where Cd^{2+} cations are coordinated by ethane-like $^{4-}$ dimers, see Fig.1a. While possessing remarkable chemical stability and favorable band edge positions for redox catalysis, bulk $CdPS_3$ is an indirect wide-bandgap semiconductor ($E_g \approx 3$ eV) [6–8], which makes it practically transparent to visible light. To unlock its catalytic potential, bandgap engineering via heterostructuring (specifically coupling $CdPS_3$ with narrow-gap sensitizers like CdS) is essential. However, conventional "wet" chemistry synthesis routes are often slow and reliant on surface-passivating ligands that block the charge transfer [9,10].

Herein, we employ a scalable, "green," and ligand-free strategy to fabricate hybrid $CdPS_3$/CdS nanostructures via femtosecond pulsed laser ablation in liquid (fs-PLAL). Unlike thermal equilibrium methods, fs-PLAL generates a high-density plasma plume confined within a cavitation bubble, creating extreme transient conditions that drive non-equilibrium phase transformations. Previously we have successfully synthesized nanoparticles from the bulk vdW and specifically TMDC crystals [11–13]. In this study, we demonstrate that solvent chemistry acts as a master switch for material design: while aqueous ablation preserves the ternary $CdPS_3$ phase, organic solvents trigger a reductive dissociation,

[a] Moscow Center for Advanced Studies, Kulakova Str. 20, Moscow, 123592, Russia. E-mail: ushkov.andrei.a@gmail.com
[b] Frank Laboratory of Neutron Physics, Joint Institute for Nuclear Research, Joliot-Curie 6, Dubna, 141980, Russia.
[c] Emerging Technologies Research Center, XPANCEO, Internet City, Emmay Tower, Al Sufouh 2, Dubai, 123592, United Arab Emirates.
[d] Department of General Physics, Perm National Research Polytechnic University, Perm, 614990, Russia.

View Article Online
DOI: 10.1039/D6NA00119J

yielding CdS quantum dots and metallic defects within the vdW matrix. This solvent-directed phase engineering results in a hybrid photocatalyst with exceptional visible-light activity toward organic pollutant degradation, establishing a versatile route for the defect-engineering of complex 2D materials.

2 Experimental

2.1 Nanoparticles synthesis via femtosecond laser ablation

Colloidal samples were produced using femtosecond pulsed laser ablation in liquid (fs-PLAL), with a bulk $CdPS_3$ crystal as the target. As is well established in the literature[14], in this technique intense laser pulses generate a plasma plume from the target, which is then trapped inside a cavitation bubble. The dynamics of this bubble's growth and implosion are critically influenced by the physicochemical properties of the liquid medium (e.g., density, heat capacity, thermal conductivity). These dynamics define the plasma condensation kinetics, which directly influence the final nanoparticle content and crystalline structure.

A ∅2 mm beam from Yb:KGW system (1030 nm, 400 fs, 10 μJ, 200 kHz, Satsuma X-28 model, Amplitude, France) was used as a source of laser radiation. The bulk crystalline target of $CdPS_3$ (dimensions: 3 × 4 × 2 mm, 2D Semiconductors Inc., Phoenix AZ, USA) was fixed vertically inside a glass chamber (BK-7, wall thickness 3 mm) filled with 5 ml of liquid media (deionized water, isopropyl alcohol, acetonitrile). Laser beam was focused on the target surface by F-Theta lens (100 mm focal distance, Thorlabs, USA) with a spot diameter $\sim$ 50 μm, corresponding to a fluence of $\sim$ 0.5 J/cm^2. To improve the synthesis productivity the liquid thickness between the target and chamber wall was minimized down to 3 mm. To avoid the ablation of a single surface spot the laser beam was continuously moved over a 2 × 2 mm area on the target surface with 3 m/s speed by galvanometric scanner (2-Axis VantagePro, Thorlabs, USA). The duration of laser ablation was 10 minutes. The NPs formation was visually detected by yellowish coloration of the initially transparent solution. The colloids remained stable after the laser ablation, showing no discernible change in color for at least one month. For storage purposes, samples were kept in closed 2 mL Eppendorf microcentrifuge tubes at a temperature of 6°C to mitigate evaporation and avoid contamination.

2.2 Sample characterization

2.2.1 Electron microscopy

Structural and morphological characterization was conducted using a high-resolution TEM (JEM 2010; JEOL) at 200 kV, utilizing a Gatan Multiscan CCD camera for both imaging (TEM imaging) and diffraction (SAED pictures) observations.

Elemental analysis and atomic composition (EDX) were assessed using a scanning TEM system (MAIA 3; Tescan) equipped with an X-act EDS detector (Oxford Instruments).

Specimens for the microscopic analysis were prepared by depositing 2 μL of the nanoparticle suspension onto a purified silicon substrate and allowing it to dry at room temperature.

2.2.2 X-ray Photoelectron and Auger Spectroscopy

High-resolution X-ray Photoelectron Spectroscopy (XPS) and X-ray induced Auger Electron Spectroscopy (XAES) were carried out on a PHI VersaProbe II 5500 spectrometer using an Al Kα X-ray source (1486.6 eV) with a primary beam spot size of 200 μm. High-resolution core-level spectra were recorded at an analyzer pass energy of 23.5 eV. The samples were prepared by drop-casting 2 mL of the nanoparticle suspension onto a cleaned silicon substrate, followed by drying at room temperature.

2.2.3 Raman spectroscopy

Raman spectroscopy was performed using a Horiba LabRAM HR Evolution system equipped with excitation wavelengths of 532 nm, a diffraction grating of 600 lines/mm, and a 100× microscope objective with a numerical aperture (NA) of 0.9. The measurements demonstrated good spectral reproducibility.

2.2.4 Photoluminescence spectroscopy

Photoluminescence spectroscopy was performed on colloidal suspensions of $CdPS_3$ nanoparticles using a BioTek Synergy H4 Hybrid Multi-Mode Microplate Reader (BioTek Instruments, Inc., Vermont, USA). Spectra were acquired at room temperature under controlled excitation conditions.

2.2.5 Photodegradation Studies

The photocatalytic performance of the synthesized $CdPS_3$ nanoparticles was assessed by tracking the degradation of methylene blue (MB) dye under 532 nm laser irradiation from a continuous-wave Nd:YAG source. To decouple the contributions of photocatalytic degradation, adsorptive loss, and direct photolysis, a comparative study was conducted across three distinct sample groups prepared in both isopropyl alcohol (IPA) and deionized (DI) water. The first group, designated the photocatalytic system, consisted of a 1 μM MB solution mixed in a 1:1 volume ratio with the $CdPS_3$ NPs colloid and was subjected to laser irradiation. The second group, the adsorption system, was prepared identically but was kept in the dark without laser exposure to quantify any dye removal due solely to adsorption onto the nanoparticle surfaces. The third group served as an MB reference control, comprising a 1:1 mixture of the MB solution and pure solvent (IPA or DI water), which was irradiated to account for direct photolytic decomposition of the dye. All reactions were monitored over a 30-minute period by periodically acquiring Raman spectra with a Horiba LabRAM HR Evolution spectrometer, allowing the degradation progress to be tracked via the temporal decay of characteristic MB Raman fingerprints.

3 Results and discussion

3.1 Laser Ablation of bulk $CdPS_3$ crystal

The experimental setup is shown in Fig.1b. The bulk crystalline target of $CdPS_3$ (2D Semiconductors Inc.) was fixed vertically inside a glass chamber filled with a liquid medium: deionized (DI) water, isopropyl alcohol (IPA) or acetonitrile (ACN). The NPs formation resulted in yellowish coloration of the colloidal solution, a characteristic optical signature of wide-bandgap semiconductor NPs ($CdPS_3$ and CdS), absorbing in the blue-UV region.

View Article Online
DOI: 10.1039/D6NA00119J

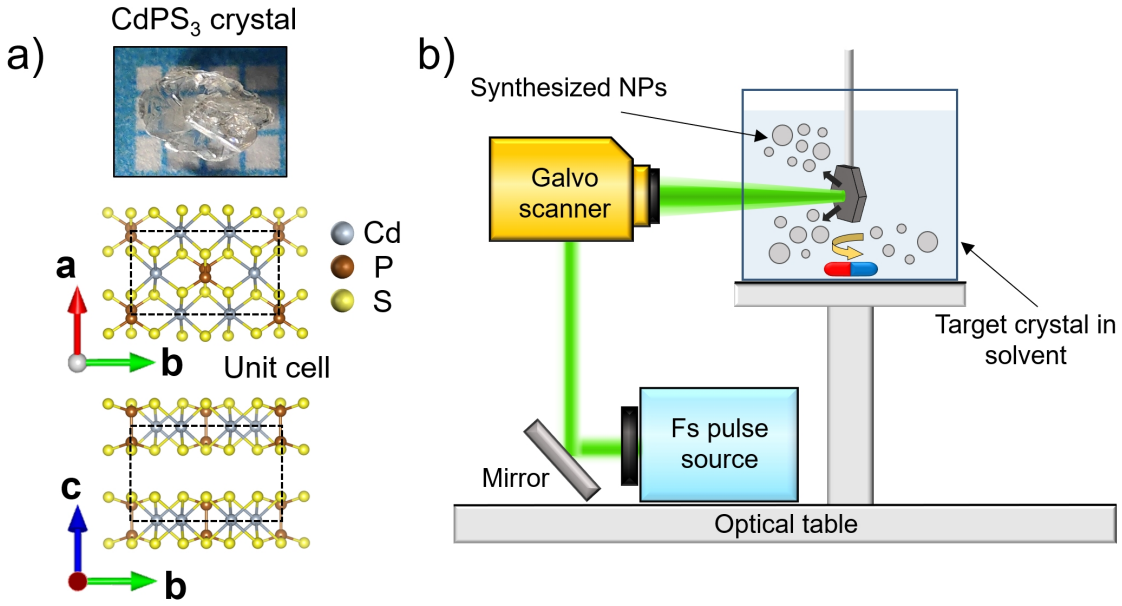

Fig. 1 (a) Crystal structure of bulk $CdPS_3$; b) Scheme of experimental setup for femtosecond pulsed laser ablation in liquid.

3.2 Morphological And Structural Characterization of PLAL-synthesized colloids

A multi-modal characterization including Transmission Electron Microscopy (TEM), Selected Area Electron Diffraction (SAED), Energy Dispersive X-ray Spectroscopy (EDX), and Raman spectroscopy was employed to elucidate the morphological, structural, and chemical properties of the colloidal nanoparticles.

Typical bright-field TEM micrographs of the colloids synthesized in DI water, ACN, and IPA are presented in Figs.2a,b,c, respectively. The images reveal polydisperse colloids (NPs diameters typically range from 10 to 80 nm) in all three samples, which is intrinsic to the PLAL mechanism - the "bottom-up" nucleation and growth of spherical nanoparticles from the laser-induced plasma plume. Notably, the particles in ACN (Fig.2b) and IPA (Fig.2c) appear to exhibit a higher degree of sphericity compared to those in water, hinting at different surface tension and cavitation bubble dynamics in organic solvents which may favor the spherodization of products prior to solidification.

The crystallinity and phase composition were probed using SAED, with corresponding patterns shown in Figs.2d,e,f. All samples display well-defined diffraction rings, confirming the crystalline nature of the nanoparticles. However, a detailed indexing of the Debye-Scherrer rings exposes a profound solvent dependency in the phase evolution.

The SAED pattern for the water-synthesized colloid (Fig.2d) corresponds to the monoclinic lattice of the parent $CdPS_3$ phase (see Supplementary Table S1 for details). This indicates that the aqueous environment facilitates rapid thermal quenching of the plasma plume. The high thermal conductivity and heat capacity of water effectively dissipate energy, kinetically trapping the ternary $CdPS_3$ stoichiometry and suppressing thermally activated decomposition or phase segregation. The oxidative potential of water does not appear to disrupt the thiophosphate framework under these conditions.

In stark contrast, the SAED patterns for ACN (Fig.2e) and IPA (Fig.2f) colloids reveal a complex superposition of diffraction signatures, including distinct reflections assignable to the hexagonal wurtzite phase of CdS. This laser-induced phase transformation highlights the critical role of the solvent environment in directing the plasma condensation pathway. Under the extreme conditions within the plasma plume, the ternary compound dissociates. During the subsequent quenching phase in organic solvents, the lower formation energy of CdS (-0.777 eV/atom) compared to $CdPS_3$ (-0.527 eV/atom) thermodynamically favors the condensation of the dissociated plasma into the more stable binary sulfide phase.

The spatial arrangement of these phases - whether they form hybrid heterostructures or exist as separate particle fractions - can be examined via spatially resolved EDX mapping. The ACN sample analysis (see Fig.2m) reveals a striking binary colloidal nature. The elemental maps for Cadmium (Cd), Phosphorus (P), and Sulfur (S) show distinct particle fractions: those rich in all three elements ($CdPS_3$) and those deficient in Phosphorus but rich in Cd and S (CdS). This spatial separation suggests that in ACN, the formation of CdS may occur within the plasma plume in parallel with formation of $CdPS_3$.

For the DI water and IPA samples, the phases were not as spatially distinct at the resolution limit of the EDX mapping, suggesting a more dense mixing or core-shell morphology. Detailed HR-TEM analysis of single nanoparticles (see Fig.2k,l) demonstrates that particles in DI water exhibit lattice fringes corresponding to the pure $CdPS_3$ phase (≈ 0.31 nm), whereas those in IPA show the coexistence of both $CdPS_3$ and CdS (≈ 0.34 nm) [15] phases within an individual NP. Although the coexistence of the $CdPS_3$ and CdS phases is evident, the exact topographical analysis of their interface is hindered by the spherical geometry of the nanoparticles, which leads to overlapping lattice projections and random zone-axis alignments in 2D HRTEM viewing. To quantify the global phase composition, a stoichiometric partitioning analysis [16] was

View Article Online
DOI: 10.1039/D6NA00119J

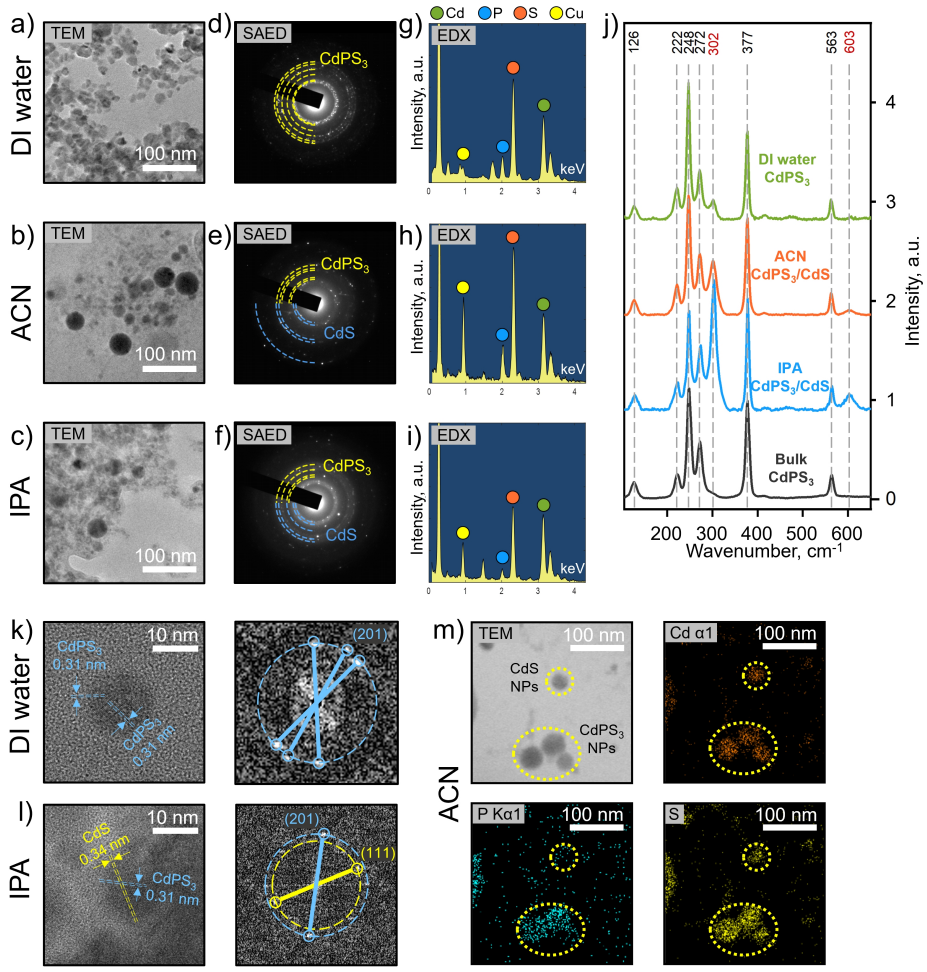

Fig. 2 Structural and elemental characterization of $CdPS_3$/CdS nanoparticles synthesized in different solvents. Typical (a-c) TEM images, (d-f) corresponding SAED patterns, and (g-i) EDX spectra of $CdPS_3$ NPs synthesized in (a, d, g) deionized (DI) water, (b, e, h) acetonitrile (ACN), and (c, f, i) isopropanol (IPA). (j) Comparison of the Raman spectra of a bulk $CdPS_3$ crystal with NPs synthesized in IPA, ACN, and DI water. (k) and (l) HR-TEM images of NPs in DI water and IPA, respectively, with corresponding FFT images, demonstrating the atomic fringes and FFT spots of $CdPS_3$ and CdS phases. m) Spatially resolved elemental analysis of NPs in ACN, demonstrating distinct $CdPS_3$ and CdS NPs.

applied to the global EDX spectra (Figs.2g,h,i). Assuming the material exists primarily as stoichiometric $CdPS_3$ and CdS[15], the molar fractions were calculated based on the atomic percentages of elements. The results are summarized in Table 1.

The data in Table 1 reveals a clear trend: the organic solvents promote the formation of CdS, with IPA being the most effective, yielding a colloid dominated by the binary phase. This is attributed to the reducing nature of IPA (a secondary alcohol), which may facilitate the abstraction of phosphorus or the stabilization of sulfur vacancies, thereby driving the equilibrium toward CdS.

Raman spectroscopy provides an additional independent confirmation of these findings. Figure 2j compares the spectra of bulk $CdPS_3$ with the colloidal samples. The bulk crystal displays sharp characteristic peaks at low wavenumbers (e.g., 248, 272, 377 cm^{-1}), corresponding to the A_{1g} and E_g modes of the metal-thiophosphate lattice ($P_2S_6^{4-}$ vibrations). The DI water sample conserves the key $CdPS_3$ modes, confirming the SAED and EDX results.

The spectra for ACN and IPA samples show a marked decrease in the intensity of the $CdPS_3$-specific modes. However, new features emerge, particularly in the 300 cm^{-1} (LO mode of CdS) and 600 cm^{-1} (2LO overtone) regions. The simultaneous observation of vibrational modes from both $CdPS_3$ and CdS in these samples confirms their biphasic content. The broadening of the peaks in the colloids relative to the bulk is attributed to phonon confinement effects in the nanocrystals and lattice strain induced by the rapid solidification.

3.3 Photoluminescence of $CdPS_3$ nanoparticles

To investigate the effects of solvent-mediated phase transformation on the electronic band structure, we performed a steady-state photoluminescence (PL) spectroscopy on the $CdPS_3$ and $CdPS_3$/CdS hybrid nanoparticles.

The photoluminescence response was initially probed using an excitation wavelength of $\lambda_{exc} = 390$ nm (3.18 eV).1 This en-

View Article Online
DOI: 10.1039/D6NA00119J

PLAL solvent	Cd, at.%	P, at.%	S, at.%	$CdPS_3$, mol. %	CdS, mol. %	RMSE, %
DI water	20.9	16.5	62.5	88.0	12.0	2.3
ACN	28.0	14.8	57.3	52.6	47.4	0.07
IPA	43.1	6.4	50.5	11.3	88.7	1.4

Table 1 Elemental content analysis of colloids, produced via femtosecond ablation of bulk $CdPS_3$ target in different solvents

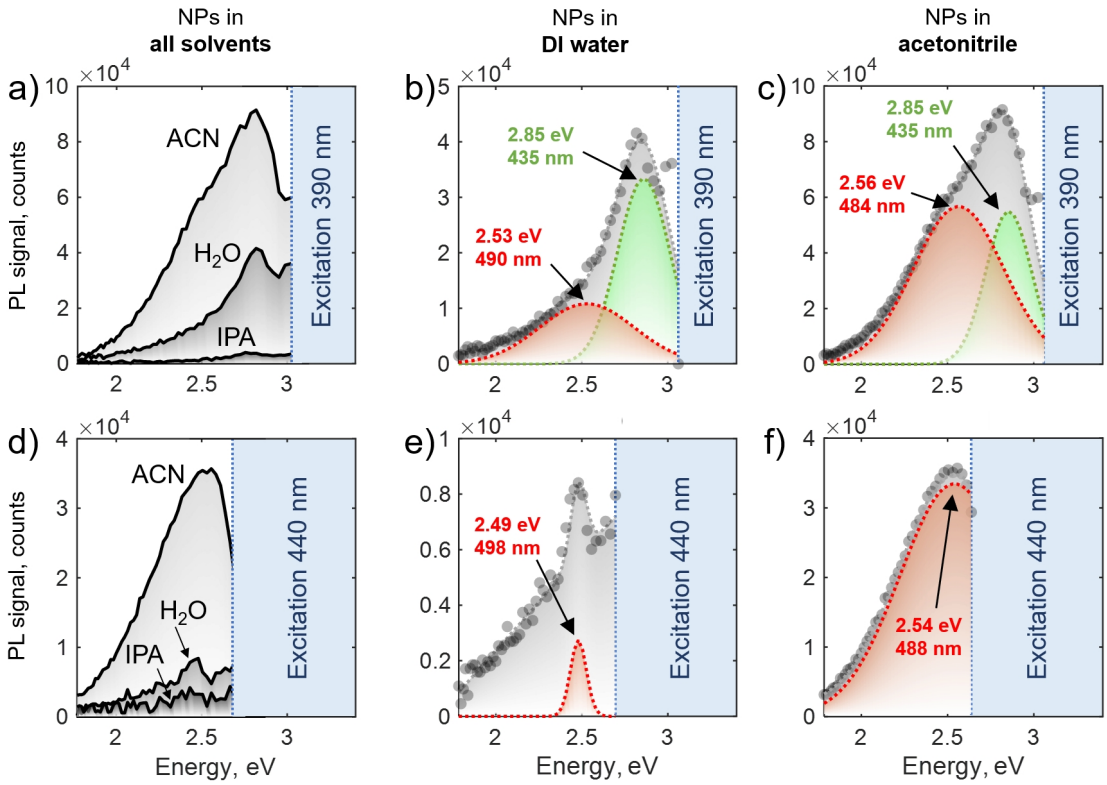

Fig. 3 Photoluminescence (PL) spectra of $CdPS_3$/CdS colloids in different solvents. a) PL of ACN, DI water and IPA colloids at 390 nm excitation; b) and c) PL signal of colloidal solutions at excitation of 390 nm in DI water and ACN, correspondingly, deconvoluted into two distinct Gaussian peaks; d) PL of ACN, DI water and IPA colloids at 440 nm excitation; e) and f) PL signal of colloidal solutions at excitation of 440 nm in DI water and ACN, correspondingly, showing a distinct Gaussian peak.

ergy was selected to be strictly suprabandgap for the bulk $CdPS_3$ phase, which possesses an optical bandgap of approximately 3 eV ($\sim$ 413 nm)[6], as well as for the binary CdS phase (bulk bandgap $\sim$ 2.42 eV)[17]. The resulting emission spectra for nanoparticles synthesized in deionized (DI) water, acetonitrile (ACN), and isopropanol (IPA) are presented in Fig.3a. All samples exhibited broad photoluminescence in the blue-green spectral region, yet the spectral profile varied significantly depending on the fs-PLAL solvent.

To decouple the overlapping contributions from the ternary parent phase and the laser-induced binary phase, we applied Gaussian deconvolution to the emission spectra. This analysis revealed two distinct channels, centered at approximately 435 nm (2.85 eV) and 490 nm (2.53 eV).

Figure 3b details the deconvolution for the DI water-synthesized colloid. The spectrum is dominated by a single emission band at 2.85 eV (435 nm). Although $CdPS_3$ is an indirect bandgap semiconductor with a low radiative efficiency, the observation of a distinct PL signal suggests the involvement of localized defect states. The non-equilibrium nature of femtosecond laser ablation, characterized by a rapid quenching rate, inevitably introduces a high density of point defects. We attribute the 2.85 eV emission to these shallow intraband defect levels, located approximately 140 meV below the conduction band edge of bulk $CdPS_3$ (3 eV). The dominance of this peak in water aligns with the structural data confirming the retention of the $CdPS_3$ stoichiometry in the aqueous environment.

In contrast, the ACN-synthesized colloid (Fig.3c) exhibits a dual-emission profile with nearly equal contributions from the 2.85 eV peak and a lower-energy band centered at 2.56 eV (484 nm). This spectral equipartition provides strong optical evidence for the formation of a binary-ternary heterostructure. The emer-

View Article Online
DOI: 10.1039/D6NA00119J

gence of the low-energy peak correlates with the appearance of CdS diffraction rings in the SAED analysis (see Fig.2e). Notably, the bulk bandgap of hexagonal CdS is 2.42 eV (512 nm). We attribute this pronounced blue shift (to 2.56 eV) to the quantum confinement effect, confirming that the segregated CdS phase comprises nanocrystals with dimensions approaching the exciton Bohr radius of CdS (~ 5.8 nm). This result indicates that the laser-induced phase transformation in ACN yields CdS quantum dots (QDs) operating within the confinement regime, mixed with the defect-rich $CdPS_3$ NPs.

By shifting the excitation wavelength to $\lambda_{exc} = 440$ nm (2.82 eV), we energetically exclude the excitation of the $CdPS_3$ host (bandgap 3 eV) and its associated shallow defects (emission 2.85 eV), while remaining well above the absorption threshold of the CdS quantum dots (~ 2.56 eV).As shown in Figs.3e,f, this selective excitation results in the complete suppression of the high-energy peak at 435 nm. The deconvoluted spectra for both ACN and IPA samples display a single Gaussian peak centered at ~ 490 nm (2.53 eV). In the DI water sample (Fig.3e) the signal is negligible, consisting primarily of background scattering, which further confirms the absence of a significant CdS phase in the aqueous synthesis. This control experiment conclusively demonstrates that the two PL peaks originate from chemically distinct species - $CdPS_3$ and CdS - rather than from multiple defect states within a single material phase.

A prominent PL feature is observed in the IPA-synthesized colloid. Although EDX analysis indicates the highest molar fraction of CdS ($\sim 90\%$) 1, its integrated PL intensity is significantly lower than that of the ACN or water samples (Figs.3a,d). Since direct-bandgap CdS quantum dots are typically highly luminescent, this suppression implies the presence of efficient non-radiative decay channels. Taking into account the strongly reducing environment provided by the alcohol solvent during the high-temperature plasma phase, the PL suppression occurs due to the the partial reduction of Cd^{2+} to metallic Cadmium (Cd^0) sites. The formation of these metallic inclusions at the interface with the semiconducting phases ($CdS/CdPS_3$) would establish Schottky-like junctions. These junctions act as efficient electron sinks, facilitating rapid spatial separation of photo-excited charge carriers. While detrimental to the PL quantum yield, this charge separation mechanism is highly advantageous for photocatalysis, as it prolongs the lifetime of reactive charge carriers. The presence of Cd^0 sites is directly confirmed by XPS analysis in Section 3.4 and is consistent with the superior photodegradation efficiency experimentally observed for the IPA sample (see Section 3.5).

3.4 XPS analysis of $CdPS_3$/CdS nanoparticles

The PL results discussed above indicate that solvent-mediated phase transformation strongly affects the electronic response of the laser-synthesized colloids. However, photocatalysis is governed not only by the bulk phase composition, but also by the chemical structure of the outermost atomic layers, where dye adsorption, charge transfer, and reactive oxygen species generation occur. Therefore, we performed X-ray photoelectron spectroscopy (XPS) and Cd MNN Auger analysis for the two limiting colloids: nanoparticles produced in DI water and in isopropanol. According to the EDX-based stoichiometric analysis in Table 1, the water-synthesized colloid is closest to the parent $CdPS_3$ phase, containing 88.0 mol.% $CdPS_3$ and only 12.0 mol.% CdS. In contrast, ablation in isopropanol yields a CdS-rich hybrid composition, with 88.7 mol.% CdS and 11.3 mol.% residual $CdPS_3$. These two samples are also compared in the photocatalytic experiments below and show strongly different degradation behavior; hence, their surface chemistry must be clarified.

High-resolution XPS spectra of Cd 3d, P 2p, and S 2p are shown in Fig.4a–f. For both colloids, the main blue doublets correspond to lattice-coordinated species. In the Cd 3d region, this contribution is assigned to Cd^{2+} bound to sulfur in Cd–S coordination, either within the preserved $CdPS_3$ lattice or within CdS domains formed during ablation in isopropanol. In addition to this main component, both samples show a weaker green Cd 3d doublet shifted to higher binding energy. This contribution is attributed to under-coordinated surface Cd atoms passivated by oxygen-containing groups generated during solvent decomposition: Cd–OH-like species in water and Cd–O–C or related alkoxide fragments in isopropanol. Thus, the Cd spectra indicate that both colloids retain crystalline Cd–S coordination, while also containing solvent-dependent surface passivation sites.

The P 2p spectra reveal a stronger difference between the two synthesis media. In the water sample, the blue doublet corresponds to lattice phosphorus in P–P and P–S bonding of the thiophosphate framework, while the additional green contribution indicates partial surface oxidation to P–O or P–OH groups. In the isopropanol sample, the P 2p envelope is more complex: besides the lattice component, green and yellow doublets appear at higher binding energies. These contributions are assigned to oxidized and amorphous phosphorus environments, including P–O–C linkages and more strongly oxidized phosphate-like species. This indicates that the thiophosphate sublattice is preferentially disrupted in isopropanol, leading to phosphorus oxidation and partial removal from crystalline $CdPS_3$ coordination.

The S 2p spectra further support this solvent-dependent surface reconstruction. The water sample shows a dominant blue doublet characteristic of lattice sulfide S^{2-} in Cd–S coordination, without pronounced high-binding-energy sulfate-like features. This points to a comparatively preserved sulfide environment at the surface. In contrast, the isopropanol sample contains, in addition to lattice sulfide, several higher-binding-energy components. The green contribution is consistent with elemental sulfur, polysulfide, or organosulfur C–S-containing fragments, while the yellow and purple components are assigned to oxidized sulfur species such as sulfite, thiosulfate, and sulfate-like groups. Therefore, the IPA-derived surface is chemically more heterogeneous, but still retains a substantial crystalline Cd–S contribution.

To compare the near-surface chemistry with the bulk elemental composition, the relative fraction of non-lattice components was extracted from the fitted XPS envelopes and compared with EDX stoichiometry, as shown in Fig.4g–i. Figure 4g summarizes the ratio between amorphous or defect-related spectral components and the total signal for Cd, P, and S. For the water-synthesized sample, this fraction remains low for all three el-

View Article Online
DOI: 10.1039/D6NA00119J

ements, indicating that the surface largely preserves crystalline coordination. For the isopropanol-derived colloid, Cd and S remain relatively close to lattice coordination, whereas phosphorus shows a pronounced amorphous contribution. Thus, the IPA sample can be described as a CdS-rich colloid with crystalline Cd–S surface motifs and strongly disordered, oxidized phosphorus species. Figures 4h,i compare stoichiometric ratios obtained from surface-sensitive XPS and bulk-sensitive EDX. For the water sample, EDX is broadly consistent with $CdPS_3$-dominated composition, although the surface shows signs of defect formation. For the IPA sample, EDX confirms a CdS-rich bulk composition, while XPS reveals that residual phosphorus is mainly present in oxidized or amorphous surface states rather than in an intact $CdPS_3$ lattice.

As the IPA-derived colloid exhibits a strong photocatalytic activity (Fig.6d), we further examined whether metallic Cd active centers are present on its surface. This is difficult to establish from Cd 3d XPS alone because the chemical shifts of Cd^0 and Cd^{2+} compounds can overlap. Therefore, Cd $M_4N_{4,5}N_{4,5}$ Auger spectra were measured for both colloids. After background subtraction and normalization to the main Cd $M_4N_{4,5}N_{4,5}$ Auger peak, the spectrum of the IPA sample shows a clear broadening on the high-kinetic-energy shoulder compared with the water sample, Fig.5a. The difference spectrum, obtained by subtracting the water-derived signal from the IPA-derived one, isolates a weak but distinct broad feature shifted toward higher kinetic energy, marked by the red arrow in Fig.5b. Such a shift is consistent with enhanced final-state screening, which is expected for Cd atoms in a more electron-rich metallic environment.

Wagner plot with both reference data for Cd-containing compounds and apparent data extracted from the measured colloids is shown in Fig.5c. The apparent points were calculated from the positions of the maxima in the Cd $M_4N_{4,5}N_{4,5}$ Auger spectra and the Cd $3d_{5/2}$ photoelectron line; the position of the difference peak was also included to evaluate the isolated high-kinetic-energy contribution. The reference data was taken from a specialized XPS literature[8,18] and outlined in Supplementary Table S2. The main signals from the water and IPA colloids fall close to the semiconducting $CdPS_3$/CdS region, confirming that most Cd atoms remain in Cd–S-based coordination. In contrast, the apparent point derived from the difference peak shifts toward the metallic Cd reference contour. This indicates that the IPA-synthesized colloid contains a minor population of Cd^0 surface sites.

The XPS/XAES results connect the solvent-directed phase transformation with the photocatalytic behavior discussed below. Ablation in water mainly preserves $CdPS_3$-like coordination, which is consistent with the weak visible-light response of this colloid. In isopropanol, the surface is transformed into a CdS-rich, defect-rich interface containing oxidized phosphorus species, organosulfur fragments, and Cd^0 active centers. The combination of visible-light-active CdS and metallic Cd sites promotes charge separation by forming local metal–semiconductor junctions, thereby suppressing recombination and facilitating interfacial electron transfer during photocatalysis.

3.5 Photodegradation properties of $CdPS_3$/CdS nanoparticles

The photocatalytic efficiency of the laser-synthesized nanoparticles was evaluated by monitoring the degradation of Methylene Blue (MB) dye, a model cationic organic pollutant, under visible light irradiation ($\lambda = 532$ nm). The kinetics of the degradation process were probed via in situ Raman spectroscopy, a technique chosen for its ability to provide molecular-level fingerprints of the pollutant concentration in real-time while distinguishing between adsorption and catalytic decomposition events. The experimental configuration, depicted in Fig. 6a, utilized a confocal Raman microscope where the excitation laser served the dual function of the actinic source for driving the photocatalytic reaction and the probe beam for acquiring the Raman scattering signal of the analyte.

To rigorously decouple the contributions of photocatalysis, physical adsorption, and direct photolysis, the study employed a comparative experimental design with three distinct sample groups for each solvent system (deionized water and IPA): (1) the Photocatalytic System (MB + NPs + Irradiation), (2) the Adsorption Control (MB + NPs in dark), and (3) the Photolysis Control (MB + Solvent + Irradiation). The degradation kinetics were quantified by tracking the intensity of the characteristic vibrational mode of the phenothiazine ring of MB at approximately 1625 cm^{-1}, which corresponds to the ν(C–C) and ν(C–N) symmetric stretching vibrations[19,20].

Fig. 6b illustrates the time-resolved Raman spectral evolution of the MB solution containing nanoparticles synthesized in IPA. A pronounced and monotonic attenuation of the MB Raman signatures, particularly the 1625 cm^{-1} band, was observed over the 30-minute irradiation period. The nearly complete disappearance of the signal indicates the rupture of the aromatic chromophore and effective mineralization of the dye. Conversely, the system containing nanoparticles synthesized in DI water exhibited negligible spectral changes under identical irradiation conditions, suggesting a lack of photoactivity in the visible spectral range.

The quantitative kinetic profiles for all sample groups are presented in Fig. 6c (DI water) and Fig. 6d (IPA). The data reveals a dramatic difference in photocatalytic performance. In the aqueous synthesis environment, the nanoparticles - previously identified as the stoichiometric $CdPS_3$ phase - showed no catalytic activity ($C/C_0 \approx 1$). This behavior is consistent with the electronic structure of bulk $CdPS_3$, which possesses an indirect bandgap[20]. In sharp contrast, the IPA-synthesized colloids demonstrated rapid degradation kinetics, with the normalized Raman intensity decreasing by approximately 90% within 30 minutes (Fig. 6d). The control experiments for this system confirmed that physical adsorption (dark) and direct laser photolysis accounted for less than 10% of the dye removal (Figs. 6c, d), attributing the majority of the degradation to the photocatalytic mechanism, consistent with previous reports on MB stability under visible light in the absence of catalysts[21]. This enhanced visible-light activity is directly correlated with the fs laser-induced phase transformation in the IPA medium. As evidenced by the structural characterization (SAED and EDX) and Raman analysis,

View Article Online
DOI: 10.1039/D6NA00119J

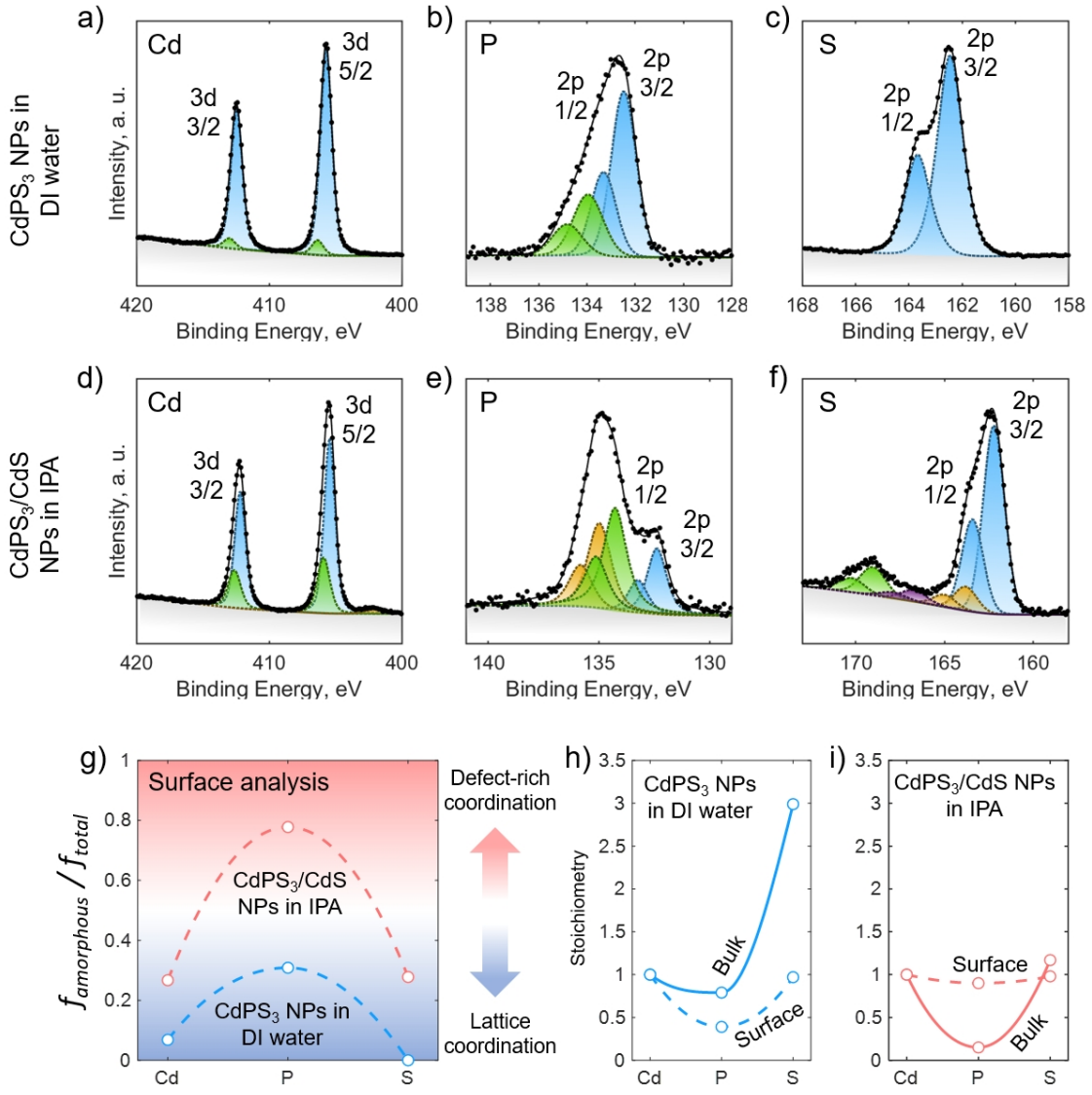

Fig. 4 XPS characterization of colloidal NPs synthesized in DI water and IPA. (a-c) Core-level photoelectron peaks of Cd, P and S elements, correspondingly, of NPs in DI water; (d-f) Core-level photoelectron peaks of Cd, P and S elements, correspondingly, of NPs in IPA; (g) The at.% ratio of amorphous, surface-oxidized states of Cd, P, S elements to their total amount for both samples, calculated via areas under corresponding photoelectron peaks; (h) and (i) bulk (EDX) versus surface (XPS) composition of nanoparticles produced in DI water and IPA, correspondingly.

ablation in IPA favors the formation of a CdS-rich phase. Cadmium sulfide, a direct bandgap semiconductor[17], effectively absorbs visible radiation, generating charge carriers[22–24].

Beyond this, the non-equilibrium fs-PLAL synthesis introduces catalytic defects. The reducing IPA medium, acting as a radical scavenger[25], facilitates partial reduction of Cd^{2+} to metallic Cd^0 domains that function as Schottky barriers at CdS surfaces[26]; the presence of Cd^0 sites is validated by XPS analysis in Section 3.4. These defects would synergize with the type-II $CdPS_3$/CdS heterojunction, creating a hierarchical charge separation architecture where Cd^0 suppresses local recombination while $CdPS_3$ mediates interfacial electron transport. The combination of phase engineering (formation of visible-light-active CdS) and defect engineering (metallic Cd sites) renders the IPA-synthesized nanoparticles highly efficient for solar-spectrum remediation applications. Although these initial degradation kinetics are highly promising, nanoscale CdS is widely known to suffer from severe photocorrosion and surface passivation during prolonged irradiation[27]. Overcoming this degradation typically requires dedicated structural engineering, such as complex Z-scheme heterojunctions, which constitutes a separate and highly specialized research direction[28]. Consequently, an exhaustive evaluation of long-term catalytic stability falls outside the primary synthesis-focused scope of this study, but it remains an objective for future optimization.

Conclusions

In summary, we have successfully demonstrated that the non-equilibrium conditions of fs-PLAL can be utilized to control the phase evolution and optoelectronic properties of the ternary vdW material $CdPS_3$ via a surfactant-free, solvent-directed strategy. By modulating the reaction environment from aqueous to or-

View Article Online
DOI: 10.1039/D6NA00119J

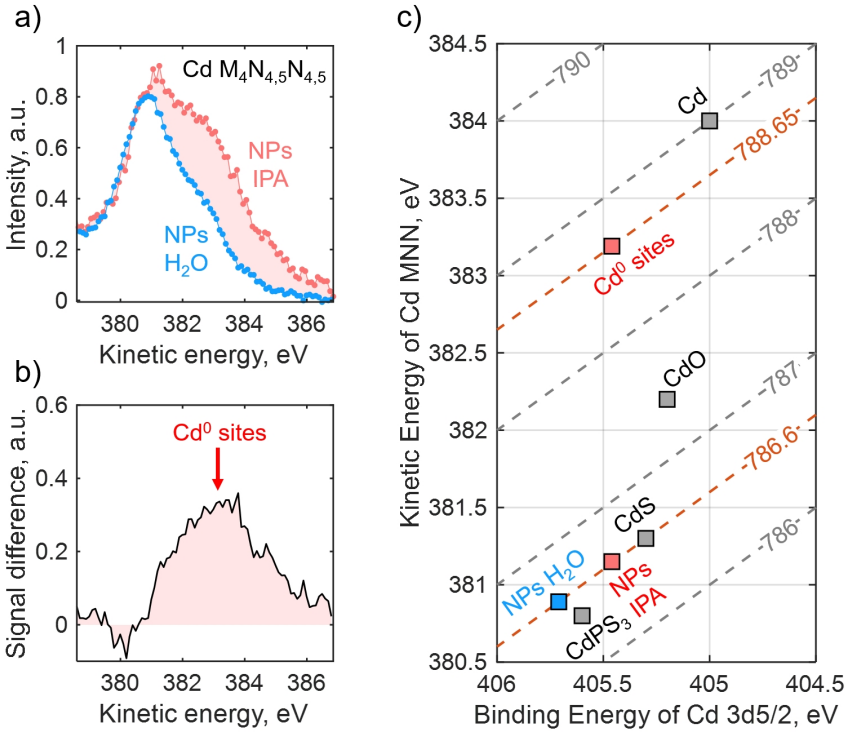

Fig. 5 XAES characterization of colloidal NPs synthesized in DI water and IPA. (a) Comparison of Auger Cd $M_4N_{4,5}N_{4,5}$ peaks, measured for NPs produced in DI water and IPA. Prior to comparison, the backgrounds were removed, and background-free spectra were normalized by their highest values. The untreated Auger spectra are shown in Supplementary Figure S1; (b) The subtraction of Auger spectra from (a), with a red arrow indicating the position of hidden Auger peak; (c) Wagner plot with positions of reference compounds ($CdPS_3$, CdS, CdO, Cd), apparent positions of DI water and IPA colloids ("NPs H_2O", "NPs IPA") and revealed position of metallic cadmium in IPA colloid ("Cd^0 sites"). Along the diagonal dashed lines the modified Auger parameter is equal, its value is indicated at every line.

ganic solvents, we achieved a tunable transition from stoichiometric $CdPS_3$ to a CdS-rich heterostructure. The reducing environment of isopropanol induced a reductive dissociation, yielding CdS quantum dots and metallic cadmium sites, transforming the UV-active host into an effective visible-light photocatalyst. The optimized hybrid material exhibited robust performance in the degradation of Methylene Blue (~90% in 30 min), attributed to enhanced visible light absorption and efficient charge separation facilitated by a hierarchical architecture of engineered junctions. This work validates fs-PLAL as a powerful, ligand-free platform for the simultaneous synthesis and phase/defect engineering of complex layered materials, providing a robust design paradigm for high-efficiency metal-thiophosphate photocatalysts.

Author contributions

A.A. supervised the project. A.U. designed the experiments and wrote the manuscript. N.B. conducted the characterizations, performed the experiments and wrote the manuscript. G.T. performed the colloidal synthesis. A.S. and S.K. conducted the TEM/SAED characterizations. S.V.B. provided experimental resources. S.N., V.G.L., G.I.T. and V.V. provided experimental resources and participated in discussions. All authors discussed the results. All authors have read and agreed to the published version of the manuscript.

Conflicts of interest

There are no conflicts to declare.

Data availability

The data supporting this article have been included as part of the Supplementary Information.

Acknowledgements

This work was funded by the RSF, project No. 25-19-00326. Maintenance of the photoluminescence spectroscopy platform was supported by the Ministry of Science and Higher Education (agreement 075-03-2025-662, project FSMG-2025-0003).

References

1 D. Li, J. C.-C. Yu, V.-H. Nguyen, J. C. Wu and X. Wang, *Applied Catalysis B: Environmental*, 2018, **239**, 268–279.
2 Y. Li, H. Chang, Z. Wang, Q. Shen, X. Liu, J. Xue and H. Jia, *Journal of Colloid and Interface Science*, 2022, **609**, 535–546.
3 E. E. Altuner, F. Gulbagca, R. N. E. Tiri, A. Aygun and F. Sen, *Chemical Engineering Journal Advances*, 2023, **14**, 100465.
4 F. Wang and M. G. Sendeku, *Nanostructured Materials for Sustainable Energy: Design, Evaluation, and Applications*, ACS Publications, 2022, pp. 1–25.
5 R. Samal, G. Sanyal, B. Chakraborty and C. S. Rout, *Journal of Materials Chemistry A*, 2021, **9**, 2560–2591.

View Article Online
DOI: 10.1039/D6NA00119J

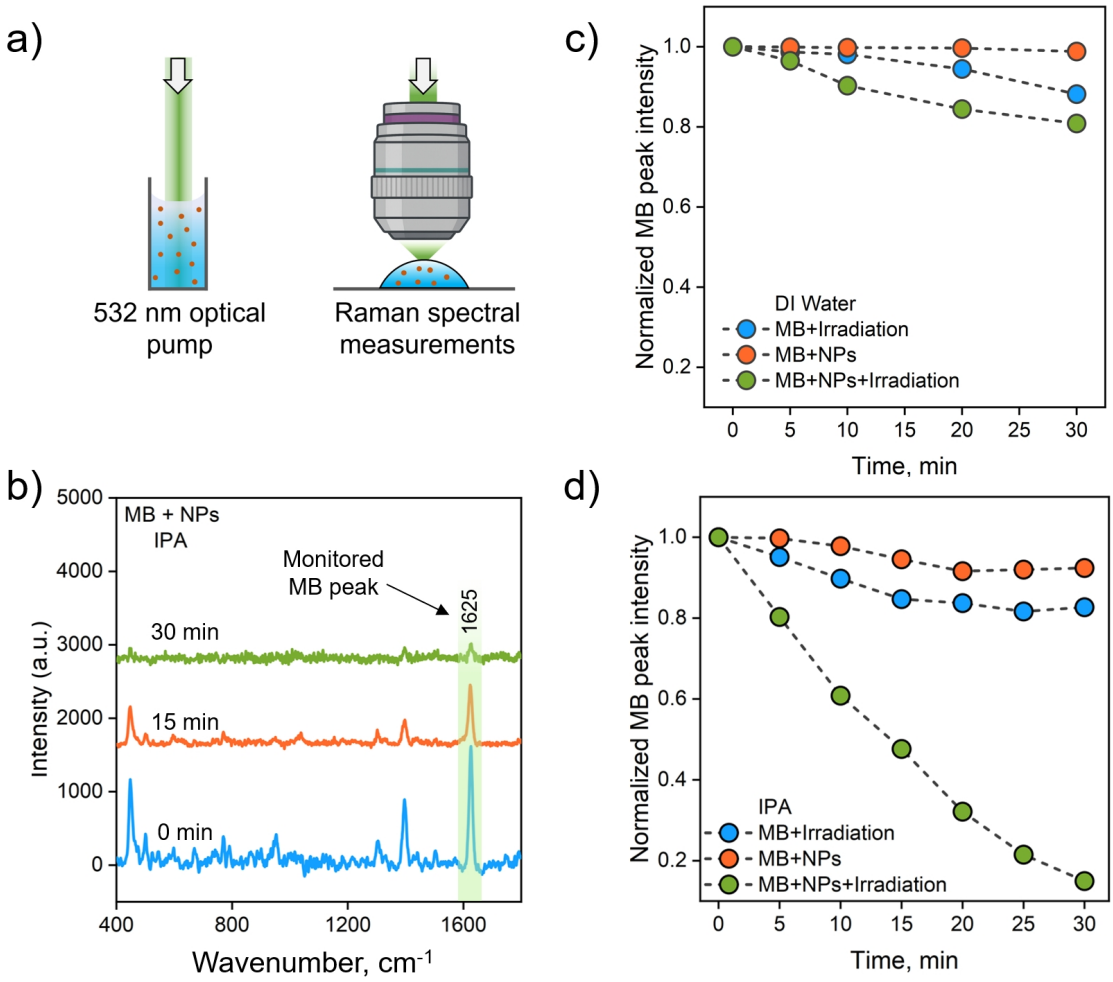

Fig. 6 (a) Schematic of the experimental setup. (b) Time-resolved Raman spectra of the photocatalytic system containing a 1:1 mixture of MB in isopropanol and a colloidal suspension of $CdPS_3$ nanoparticles. (c, d) Intensity of the MB Raman peak at 1625 cm^{-1} as a function of time for samples in different solutions: (c) DI water and (d) IPA.

6 H. Li, N. Wells, B. Chong, B. Xu, J. Wei, B. Yang and G. Yang, *Chemical Engineering Science*, 2021, **229**, 116069.
7 C. Calareso, V. Grasso and L. Silipigni, *Journal of applied physics*, 1997, **82**, 6228–6234.
8 G. Curro, V. Grasso and L. Silipigni, *Journal of applied physics*, 1998, **84**, 6693–6697.
9 A. R. Rothfuss, J. R. Ayala, J. V. Handy, C. R. McGranahan, K. E. Garcia-Pedraza, S. Banerjee and D. F. Watson, *ACS Applied Materials & Interfaces*, 2023, **15**, 39966–39979.
10 P. Bhavani, D. P. Kumar, M. Hussain, W.-H. Chen, S. S. Lam and Y.-K. Park, *Fuel*, 2023, **334**, 126551.
11 G. I. Tselikov, A. A. Minnekhanov, G. A. Ermolaev, G. V. Tikhonowski, I. S. Kazantsev, D. V. Dyubo, D. A. Panova, D. I. Tselikov, A. A. Popov, A. B. Mazitov *et al.*, *ACS nano*, 2025.
12 G. I. Tselikov, G. A. Ermolaev, A. A. Popov, G. V. Tikhonowski, D. A. Panova, A. S. Taradin, A. A. Vyshnevyy, A. V. Syuy, S. M. Klimentov, S. M. Novikov *et al.*, *Proceedings of the National Academy of Sciences*, 2022, **119**, e2208830119.
13 A. Ushkov, D. Dyubo, N. Belozerova, I. Kazantsev, D. Yakubovsky, A. Syuy, G. V. Tikhonowski, D. Tselikov, I. Martynov, G. Ermolaev *et al.*, *Nanomaterials*, 2024, **15**, 4.
14 D. Zhang, B. Gokce and S. Barcikowski, *Chemical reviews*, 2017, **117**, 3990–4103.
15 M. G. Sendeku, K. Harrath, F. T. Dajan, B. Wu, S. Hussain, N. Gao, X. Zhan, Y. Yang, Z. Wang, C. Chen *et al.*, *Nature Communications*, 2024, **15**, 5174.
16 J. I. Goldstein, D. E. Newbury, J. R. Michael, N. W. Ritchie, J. H. J. Scott and D. C. Joy, *Scanning electron microscopy and X-ray microanalysis*, springer, 2017.
17 S. Sze, *CA Mead, Analog VLSI and Neural Systems (Addison-Wesley, Reading, MA*, 1989, 2959–2964.
18 J. Chastain and R. C. King Jr, *Perkin-Elmer Corporation*, 1992, **40**, 25.
19 J. C. Rubim, M. H. Sousa, J. C. Silva and F. A. Tourinho, *Brazilian Journal of Physics*, 2001, **31**, 402–408.
20 X. H. Vu, N. D. Dien, T. T. H. Pham, T. T. Trang, N. Ca, P. Tho, N. D. Vinh and P. Van Do, *RSC advances*, 2020, **10**, 38974–38988.
21 M. Rauf and S. S. Ashraf, *Chemical engineering journal*, 2009, **151**, 10–18.

View Article Online
DOI: 10.1039/D6NA00119J

22 L. Cheng, Q. Xiang, Y. Liao and H. Zhang, *Energy & Environmental Science*, 2018, **11**, 1362–1391.

23 J. A. Nasir, Z. ur Rehman, S. N. A. Shah, A. Khan, I. S. Butler and C. R. A. Catlow, *Journal of Materials Chemistry A*, 2020, **8**, 20752–20780.

24 L. Zhang, Z. Ai, X. Xu, D. Shi, B. Zhang, H. Hu, M. Yang, Y. Shao, Y. Wu and X. Hao, *Ionics*, 2023, **29**, 2115–2139.

25 K. Pitchumani and M. Kumarraja, *Reducing Agents in Colloidal Nanoparticle Synthesis*, The Royal Society of Chemistry, 2021, p. 1.

26 R. Li, Z. Dai, T. Huang, Q. Zhang, X. Zhou, Z. Peng, Z. Liu and Y. Fang, *Surfaces and Interfaces*, 2024, **45**, 103926.

27 Y. Chen, W. Zhong, F. Chen, P. Wang, J. Fan and H. Yu, *Journal of Materials Science & Technology*, 2022, **121**, 19–27.

28 L. Li, J. Luo, L. Chen and J. Shi, *ACS Sustainable Chemistry & Engineering*, 2023, **11**, 16703–16712.

View Article Online
DOI: 10.1039/D6NA00119J

The data supporting this article have been included as part of the Supplementary Information.